Deciphering the Role of Water in Promoting the Optoelectronic Performance of Surface-Engineered Lead Halide Perovskite Nanocrystals

Harshita Bhatia, Cristina Martin, Masoumeh Keshavarz, Iurii Dovgaliuk, Nadine J. Schrenker, Martin Ottesen, Weiming Qiu, Eduard Fron, Martin Bremholm, Joris Van de Vondel, Sara Bals, Maarten B.J. Roeffaers, Johan Hofkens, and Elke Debroye*

ABSTRACT: Lead halide perovskites are promising candidates for high-performance light-emitting diodes (LEDs); however, their applicability is limited by their structural instability toward moisture. Although a deliberate addition of water to the precursor solution has recently been shown to improve the crystallinity and optical properties of perovskites, the corresponding thin films still do not exhibit a near-unity quantum yield. Herein, we report that the direct addition of a minute amount of water to post-treated formamidinium lead bromide ($FAPbBr_3$) nanocrystals (NCs) substantially enhances the stability while achieving a 95% photoluminescence quantum yield in a NC thin film. We unveil the mechanism of how moisture assists in the formation of an additional NH_4Br component. Alongside, we demonstrate the crucial role of moisture in assisting localized etching of the perovskite crystal, facilitating the partial incorporation of NH_4^+, which is key for improved performance under ambient conditions. Finally, as a proof-of-concept, the application of post-treated and water-treated perovskites is tested in LEDs, with the latter exhibiting a superior performance, offering opportunities toward commercial application in moisture-stable optoelectronics.

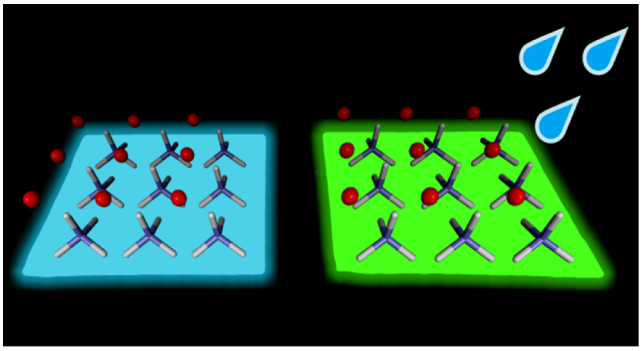

KEYWORDS: *lead halide perovskites, surface defects, passivation, post-treatment, nanocrystals, light-emitting diodes, spectroscopy*

1. INTRODUCTION

Organic−inorganic lead halide perovskites (LHPs) exhibit outstanding optoelectronic properties for light harvesting and emission devices.[1−3] However, the function of the perovskite layer in these distinct applications differs fundamentally. 3D $APbX_3$ (where A is an organic or inorganic cation, and X is a halide) LHPs possess large absorption coefficients, long charge carrier diffusion lengths, and small exciton binding energies (E_b), which are highly desirable for solar cell applications.[4] In contrast, light-emitting diodes (LEDs) benefit from a high E_b, which is not commonly observed in traditional 3D perovskites.[5] Despite this limitation, significant progress in photoluminescence (PL) efficiency has been achieved, owing to the high defect tolerance, color purity, and a wide range of color tunability of 3D perovskites.[5] However, 3D LHP-based devices lack long-term stability, restricting their commercialization.

Recently, 2D A_2PbX_4 LHPs have gained considerable attention due to their remarkable stability compared to their 3D counterparts.[6,7] Furthermore, these structures exhibit appealing properties, such as a strong quantum and dielectric confinement, which results in a high E_b, making them attractive for electroluminescence (EL) applications.[8] However, high external quantum efficiencies (EQE) have not yet been achieved for LEDs based on "pure 2D" perovskites due to the presence of large organic insulating ammonium cations, restricting their charge transport properties.[1,2] Hence, the formation of a 2D/3D heterostructure (also known as quasi-2D perovskites) is a valuable method to combine the best of both worlds, that is, structures with enhanced stability and spatially confined carriers while maintaining optimum charge carrier transport.

Multiple studies have shown that the surface of LHP nanocrystals (NCs) exposes a large number of dangling bonds owing to their large surface-to-volume ratio, which traps a fraction of charge carriers, serving as non-radiative recombi-

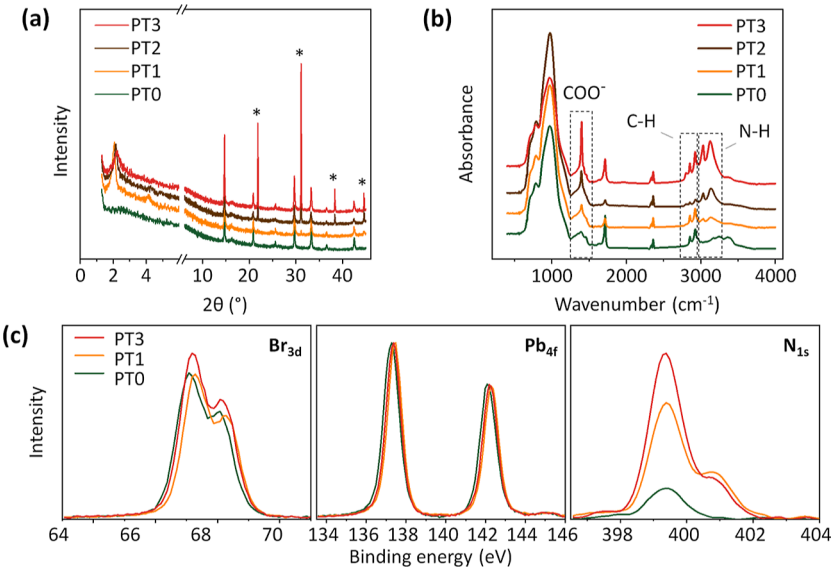

Figure 1. (a) XRD, (b) FTIR, and (c) XPS spectra of untreated and post-treated $FAPbBr_3$ NCs. The symbol (*) in (a) indicates the NH_4Br cubic phase. The XPS spectra are normalized to their respective Pb 4f peaks.

nation centers.[9] Moreover, surface defects also promote the penetration of moisture and accelerate the degradation of perovskites.[10] Recently, several studies have demonstrated effective strategies to passivate the LHP NC surface, promoting radiative recombination, for example, by introducing bulky organic surfactants such as ammonium tetrafluoroborate, diammonium halides, silver−trioctylphosphine complexes, didodecyl dimethylammonium fluoride, and so forth.[11−15] Some reports find MA I-[16,17] or FABr-rich[18,19] conditions to be beneficial for device performance as their excess may passivate defects at the surface. Besides these typical passivation strategies, the incorporation of water in the ligand-assisted re-precipitation (LA RP)reaction mixture has also been demonstrated to play a positive role in controlling the morphology and stability of LHP NCs.[20,21] Other studies have demonstrated that a minute amount of water as a solvent additive promotes the formation of uniform LHP NC films, inducing higher stability and improved optoelectronic properties.[22,23] Despite these remarkable advancements, practical applications are still hampered by the limited stability of the resulting LHP NC films under ambient conditions.

Herein, we developed a novel post-treatment strategy that could allow the utilization of perovskite NCs in moisture-stable optoelectronics. We started off with a single-step synthesis of $FAPbBr_3$ NCs using synergistic ligands, short-chain *sec*-butylamine (*s*-BA),and oleic acid (OA c).We first discuss the structural and optical characteristics of the as-prepared FA $PbBr_3$ NCs. Further, we modify the surface chemistry of NCs by applying a facile post-treatment strategy, using extra molar equivalents of FA Br in hexane-containing ligands. The slow intrusion of atmospheric moisture hydrolyzes the excess FABr from the post-treatment reaction mixture, leading to the formation of formamide and surface-stabilizing ammonium bromide (NH_4Br). The high concentration of $NH_4^+Br^-$ resulted in NCs with higher stability and substantially improved optical properties, displaying a high PL quantum yield (PLQY) of 85% when deposited as device-ready NC thin films. Additionally, this work also explores the effect of directly adding minute amounts of water [0.2% (v/v)] to the post-treated FA $PbBr_3$ NCs. While earlier studies have demonstrated the role of water in facilitating the phase transformation (Cs_4PbBr_6 to $CsPbBr_3$ or $CsPbBr_3$ to $CsPb_2Br_5$),[24,25] influencing the growth rate and shape of NCs,[26] structural reorganization,[27] and surface crystallization,[28] this study elucidates its role in locally exfoliating and etching the post-treated NCs, thereby creating possible channels for the intercalation of NH_4^+ cations as well as promoting the self-assembly of NCs. This, consequently, promotes the stabilization of the NCs, raising the PLQY to 95% when deposited as thin films. Finally, as a proof-of-concept, the application of post-treated and water-treated FA $PbBr_3$ NC thin films was explored in LEDs. Strikingly, the water-treated LHPs exhibited up to 3 times higher EQE as compared to solely post-treated FA $PbBr_3$ NCs.

2. RESULTS AND DISCUSSION

FA $PbBr_3$ NCs are synthesized by a facile, ligand-mediated, wet chemical approach. First, a stoichiometric ratio of FA Br and $PbBr_2$ is dissolved in *N*-dimethylformamide (DMF). Meanwhile, a mixture of synergistic ligands, *s*-BA and OAc, is added to the antisolvent, toluene. Finally, the injection of the precursor into the toluene solution yields a blue-green emissive suspension under UV illumination. This blue-green emission is a typical feature of low-dimensional perovskites. Herein, a low-dimensional (quasi-2D) structure is suspected to be generated by the formation of *sec*-butylammonium, which will be clarified later. However, the emission color rapidly changes from blue-green to green and readily loses intensity as soon as the NCs are washed with toluene, suggesting a structural change in ambient conditions. In an attempt to maintain the initial quasi-2D structure with the appealing blue-green emission, we employ a surface passivation strategy. Immediately after synthesis, the NCs are sonicated with extra molar equivalents of FA Br (employed in the post-treatment mixture), manifest-ing a positive effect on the stability and allowing the $FAPbBr_3$ NC suspension to retain the initial bright blue-green emission. More specifically, the samples are post-treated with 0.02 (1 equiv), 0.04 (2 equiv), and 0.06 mmol (3 equiv) of FABr dissolved in hexane containing OA c and oleylamine (OAm), which are hereafter referred to as PT1, PT2, and PT3,

Scheme 1. Structural Evolution of $FAPbBr_3$ NCs (i) before and after Treatment and (ii) when the Structures are Exposed to Moisture; Blue Cations in (ii) Depict NH_4^+

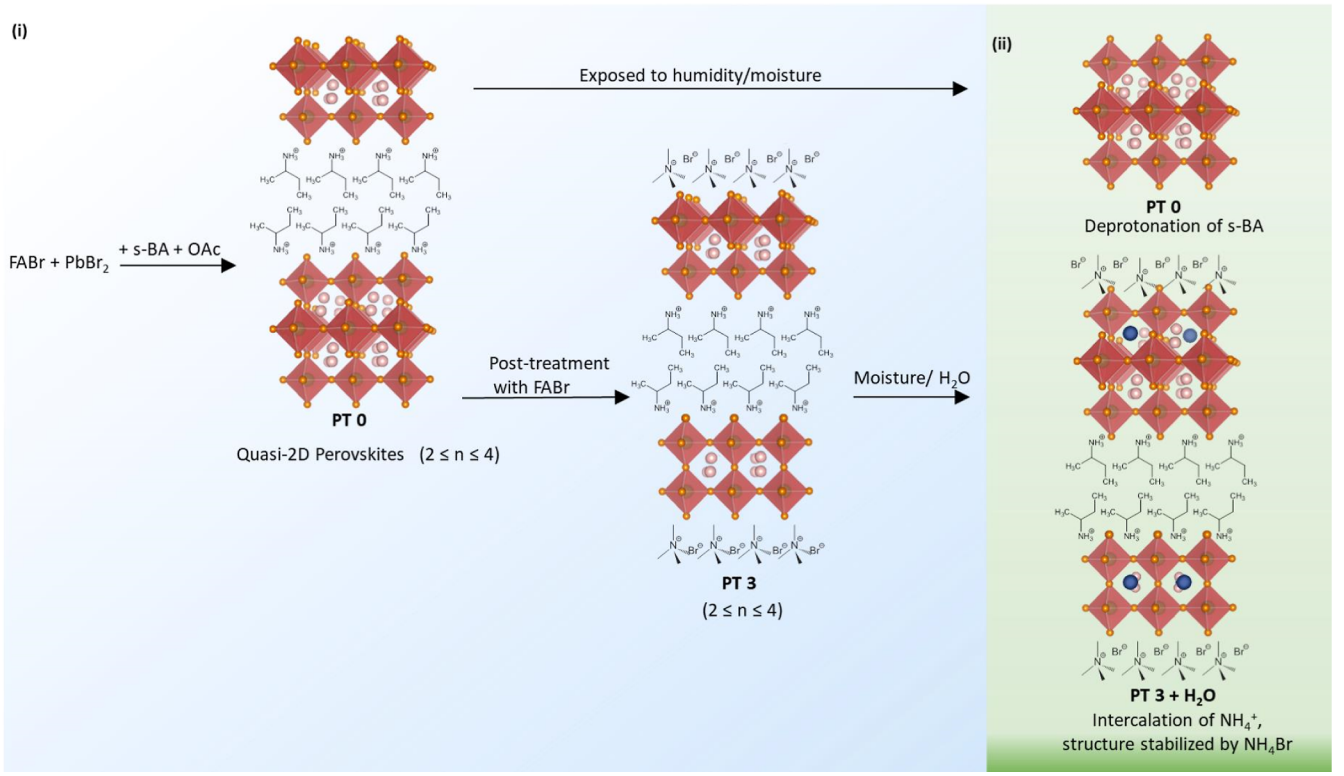

respectively. The untreated sample is referred to as PT0. A more detailed explanation of the protocol is discussed in the Experimental Procedure. Moreover, the effect of humidity on the NCs' structure has been investigated, and the representative structural change upon post-treatment is schematically demonstrated. Following the synthesis and post-treatment, the structure is evaluated using transmission electron microscopy (TEM), X-ray diffraction (XRD), grazing incidence XRD (GIXRD), X-ray photoelectron spectroscopy (XPS), and Fourier-transform infrared spectroscopy (FTIR) techniques, while the optical properties are investigated using steady-state and time-resolved PL. Note that all characterizations were performed in thin film form by simply dropcasting the NC suspension on a glass slide or TEM graphene grids.

2.1. Structural Properties. As shown in Figure 1a, PT0 was formed with the conventional $FAPbBr_3$ cubic phase.[18] However, upon post-treatment (i) four extra peaks appear, which get more pronounced when applying higher molar equivalents of FABr. XRD refinement reveals the presence of a mixture of two cubic phases, the major phase corresponding to the typical cubic structure of $FAPbBr_3$ [$Pm\bar{3}m$, a = 6.0179 (2) Å],[29] and a second phase with sharp peaks (marked with *) belonging to the cubic ammonium bromide (NH_4Br) structure [$Pm\bar{3}m$, a = 4.0620 (1) Å] (Figure S1).[30] (ii) The XRD patterns of the post-treated $FAPbBr_3$ NCs exhibit low-angle diffraction features below $2\theta = 15°$, suggesting the presence of a low-dimensional structure, which is potentially further stabilized by the presence of NH_4Br. It is important to note that post-treatment is generally a surface modifying (healing in this case) approach and is not expected to impact the bulk of the crystal. Considering the fact that the XRD pattern reveals highly intense peaks corresponding to the cubic phase of NH_4Br, it is anticipated that some part of the NH_4Br interacted with the crystal surface, assisting in stabilizing and preserving the dimensionality of the NCs, whereas another fraction remained as "free"-NH_4Br in the structure, exhibiting an additional phase.

First, our attention will be focused on the elucidation of the appearance of the additional NH_4Br cubic phase. For the post-treatment, we employed different molar amounts of FABr, mixed with OA c and OA m capping ligands in hexane. The trace of water present in hexane solution from the atmosphere most likely induces the base (OA m)-catalyzed hydrolysis of FA Br, leading to the formation of formamide and NH_4Br (Scheme S1). As control experiments, the XRD patterns of a mixture of FABr and water as well as a mixture of FABr, OAm, and water were recorded (Figure S2). The latter composition revealed an XRD pattern corresponding to the NH_4Br cubic phase, as is also observed for the post-treated NCs, thus confirming our hypothesis.

To study the influence of formamide on the structure, additional control experiments were performed, where the NCs were post-treated with a mixture of NH_4Br and a varying amount of formamide (Figure S3). It was observed that formamide, as such, has no impact on the perovskite structure, but it mainly aids in the dispersion of the NH_4Br salt, attributing to its polar nature (refer Supporting Information for more info, Figure S3). We anticipate a higher production of formamide with increasing molar equivalents of FABr, which is also evident in the FTIR spectrum (Figure 1b) and will be discussed hereafter.

Next, more detailed GIXRD measurements (Figure S4) resulted in five reflections in the low 2θ region at around 2.4, 4.7, 9.5, 11.8, and 14.4° (corresponding to a lattice spacing up to $d \approx 36.7$ Å). These reflections cannot arise from an oriented 3D LHP structure since they are located too low in the 2θ

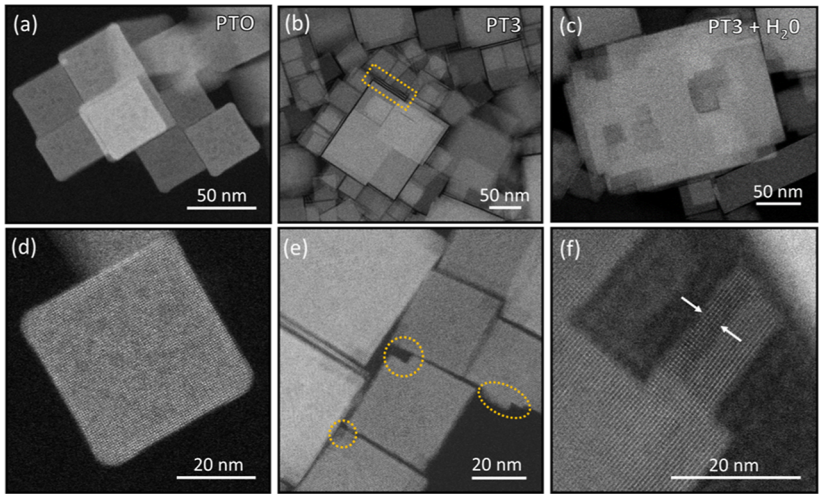

Figure 2. HAADF-STEM images of (a) PT0, (b) PT3, and (c) PT3 + H2O. In (b), thin NCs that are oriented edge-on and are stacked on top of each other are highlighted with a yellow rectangle. This indicates the presence of low-dimensional perovskite NCs. (d) PT0, (e) PT3, and (f) PT3 + H2O are the corresponding high-magnification images; yellow circles in (d,e) highlight exfoliated and etched spots. The arrows in (f) indicate the step-like structure, where etching resulted in a step with a width of ∼4 nm.

region and thus confirm the presence of a low-dimensional structure, as previously observed for other perovskites.[31] In particular, the peak positions of these low-angle features reflect an $n \leq 4$ composition, where n is the number of layers of $FAPbBr_3$ unit cells, as it is expected that an $n = 4$ composition contain peaks from $n = 1-3$ structures. For $n \geq 4$ structures, the diffraction peaks representing smaller n values would be very weak or would even completely disappear.[31] At this point, it is anticipated that the organic spacer that assists the formation of the quasi-2D structure is *sec*-butylammonium, which is formed after the protonation of *s*-BA by OAc in the aprotic solvent.[32] The large *d*-spacing value is thus attributed to this bulky cation participating in the formation of the quasi-2D structure [Scheme 1, left panel (i)].

To further verify the above-stated findings, FTIR and XPS measurements were conducted on the untreated and post-treated NCs. In Figure 1b, the FTIR spectrum features sharp absorption bands at ∼2860 and 2930 cm^{-1}, which are assigned to the asymmetric stretching vibrations of CH_2 and CH_3 of the capping ligands, respectively. Additionally, two distinct peaks around ∼3050 and 3150 cm^{-1} appear, corresponding to the stretching vibrations of ammonium, originating from protonated *s*-BA and NH_4^+.[33] Notably, these peak intensities are relatively increase for the samples post-treated with increasing molar equivalents of FA Br, implying the presence of more ammonium species, including free-standing NH_4Br. This finding is in line with the obtained XRD data, displaying the highest peak intensities reflecting the NH_4Br phase for the PT3 NCs. Furthermore, the post-treated films exhibited a gradual increase in the band around 1713 cm^{-1}, which may be assigned to the C═O stretching mode of formamide. However, this peak can also be observed as a result of C═O or C═N stretching of the carboxylic group of OAc or of FA^+, respectively (Figure S5). It is certainly difficult to assign the exact contribution; however, it can only be speculated that the increase in the intensity of peaks around 1713 cm^{-1} for the post-treated NCs could more likely be attributed to the formation of formamide, the amount of which increases with increasing molar amounts of FABr, as also noted for the XRD pattern. It is less likely to be arising from carboxylic acid as its contribution is expected to decrease on account of proton transfer between an excess of OAc and OAm or *s*-BA, supplied during the post-treatment step. Additionally, the desorption of ligand (unbound OAc) could also be attributed to the additional washing step, specifically performed for the post-treated NCs.[34] Consequently, the deprotonation of OAc increases the relative intensity of the COO^- band, having symmetric and asymmetric modes around ∼1400 and 1467 cm^{-1}, respectively. The difference between these two characteristic bands is ∼67 cm^{-1}, reflecting a bidendate coordination of OA cto Pb^{2+}.[35] This indicates that oleate anions are also adsorbed on the perovskite surface, further passivating the surface defects (undercoordinated Pb^{2+}).[36] Notably, a considerable amount of unbound carboxylic acid remained in the suspension of PT0, probably due to the limited washing steps. Moreover, the PT0 NCs lacked an excess of ligands (absence of post-treatment step) to undergo any further protonation−deprotonation reaction, and hence, the trend in the intensity of the peaks, at 1400 and 1700 cm^{-1}, is opposite to the post-treated ones. The FTIR spectra of all the control samples can be consulted in the SI, Figure S5.

In line with this, XPS measurements revealed a gradual increase in the intensity ratio of N/Pb and Br/Pb at the surface of the $FAPbBr_3$ NCs upon post-treatment. Figure 1c represents the high-resolution XPS spectra of Pb 4f, Br 3d, and N 1s core levels for the untreated perovskites and post-treated perovskites. The acquired spectra possess consistent chemical features for all the samples, with no remarkable difference in the peak position. In order to evaluate the changes in the chemical composition after post-treatment, the spectra for Br 3d and N 1s were normalized with respect to the Pb 4f peak, revealing a substantial difference in intensity of the Br 3d and N 1s peaks for the post-treated $FAPbBr_3$ NCs, especially for PT3 when compared to that of PT0. The gradual increase in the intensity ratio of N/Pb from PT0 to PT3 confirms the presence of an excess of the ammonium cation at the NC surface, as previously suggested by XRD and FTIR. This is further supported by the N 1s XPS spectra, where two peaks are observed for the post-treated samples, one at ∼399 eV, belonging to pristine amine (*s*-BA), and another one at ∼401 eV, belonging to the corresponding protonated amine (i.e., $-NH_3^+$ or NH_4^+), which is absent for PT0.[37] So far, the results

from XRD, XPS, and FTIR collectively indicate that some fraction of ammonium is tethered to the surface of the post-treated NCs and some remained as free-NH_4Br, acting as a passivating entity and promoting stability. Additionally, Br/Pb also increased from 2.8 to 3.7 upon post-treatment due to the additional NH_4Br layer. Notably, the halide-rich circumstances are also beneficial for obtaining high-quality perovskite NCs, owing to the self-passivation effect.[18,38] The atomic ratios of Br/Pb and N/Pb for perovskites PT0, PT1, and PT3 are given in Table S1.

Furthermore, we performed high-angle annular dark-field scanning transmission electron microscopy (HAADF−STEM) at low magnification with a low electron beam dose to examine the morphology of untreated and treated NCs (Figure 2a−c). The high-resolution STEM images are also displayed in Figure 2d−f. The STEM images for PT0 and PT3 exhibit a uniform cubic morphology, possessing an average edge length of 25−50 nm (Figure S6). The fast Fourier transform (FFT) of a high-resolution STEM image of PT0 NCs (Figure S7) shows the NCs are oriented in the [100] zone axis (ZA). While the majority of PT3 NCs exhibited a horizontal orientation, a fraction of them were also found to be aligned edge-on (Figure 2b, marked with a yellow rectangle), highlighting the existence of lower dimensional structures. Notably, no specific substrate-induced reorientation could be identified.[2,39] Furthermore, the vertically aligned crystals exhibited an average thickness of ∼1.2−1.8 nm (Figure S8), which is in excellent agreement with the calculated thickness of nanoplatelets having n = 2 (1.2 nm) and n = 3 (1.8 nm).[40] Notably, edge-to-edge stacking was not observed for PT0 NCs. Additionally,the PT3 NCs also displayed unusual, partially etched corners (Figure 2e, marked with yellow circles). Such structural features could be induced either by the interaction of the highly energetic electron beam,[41] or by polar solvents,[42] which tend to dissolve or decompose the perovskites. Notably, in this study, the e-beam dose was kept extremely low in order to avoid the beam damage. Considering that the etching effect is not seen for PT0 NCs, following the similar conditions, we exclude the e-beam being the cause for the repercussion. To further probe the etching mechanism, we attempted to react PT3 NCs with a minute amount of water (denoted as PT3 + H_2O, hereafter). Interestingly, a tiny drop of water, 0.2% (v/v), instantly changed the emission color from blue-green to a highly emissive green, which is in line with what we will discuss later. It is anticipated that the interaction of perovskite NCs with an extremely small amount of water leads to chemical dissolution,[43] formally releasing the constituent ions of $FAPbBr_3$ (FA^+, Br^-, Pb^{2+}) from the surface. Notably, the dissolution seems to take place at preferential sites instead of exhibiting a uniform dissolution of the crystal (Figures S8 and S9). Consequently, small etch-pits of different dimensions emerge throughout the crystal, mainly at the edges (Figure 2e,f). We propose that the removal of constituent ions creates an initial weak point in the crystal lattice, forming initiation sites for the etching process (as seen in Figure 2e), which subsequently broadens over time, forming a step-like structure, as evident for water-treated perovskites (Figure 2f). The NCs self-assemble to form a stack-like morphology (Figure 2c). Furthermore, we also observed a few thin square- and rectangular-shaped flakes, which are likely exfoliated from the edges of the crystals (Figure S9 and Scheme S2), stemming from the weak van der Waals interaction between the interlayers.[44] Typically, such structural inhomogeneity is found after etching; this can either induce heterogeneity in the structural and optical properties[45] or could assist in forming new structures [e.g., from platelets (2D) to quantum dots (0D)].[42] Lastly, we point out that the exfoliated regions formed upon water addition do not exhibit any obvious defects (Figure 2f), implying that the perovskites' cubic structure was retained (cfr. XRD), which is also consistent with FFT patterns.

Next, from the XRD data, we could clearly resolve the cubic phase of $FAPbBr_3$ and NH_4Br in PT3 and PT3 + H_2O (Figure 1a). However, in contrast, the electron diffraction pattern only identified the cubic $FAPbBr_3$ phase (Figure S10). Notably, we spotted a large sphere covering the top of PT3 + H_2O NCs, which could be ascribed to the free-standing NH_4Br, according to EDX data (Figure S11). Additionally, considering the fact that hexane is an antisolvent to NH_4Br, it tends to have high surface energy in hexane. To minimize the surface area, the particles are anticipated to take the form of a sphere, and thus, we ascribe the spherical particle to NH_4Br.[46] However, crystallographic data could not be locally resolved.

2.2. Photophysical Properties. In this section, we evaluate the optical properties of the untreated and post-treated NCs, dropcasted in thin film form. The normalized UV−vis absorption (dashed lines) and PL spectra (solid lines) are shown in Figure 3. As seen in Figure 3a, PT0 exhibits two

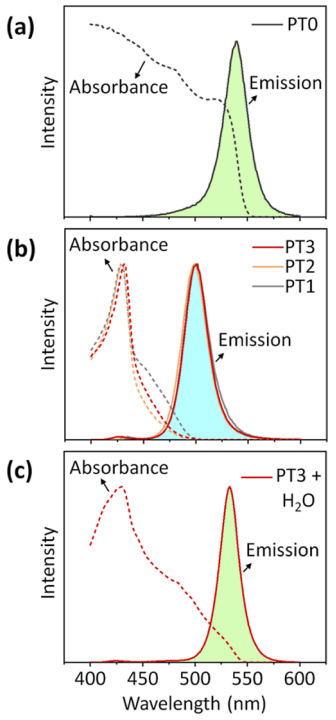

Figure 3. PL and absorption spectra of (a) PT0, (b) post-treated $FAPbBr_3$ NCs (day 1), and (c) PT3 + H_2O.

features in the absorption spectrum at 450 and 479 nm, with an absorption edge at 528 nm. When excited at 395 nm, the PL spectrum exhibits an emission maximum at 539 nm with a narrow full width at half-maximum (fwhm) of 30 nm. Also, there is a very weak emission band (475−500 nm) in the tail of the main peak, which corresponds to the additional features in the absorption spectrum. This optical performance indicates that PT0 mainly adopts a 3D perovskite structure and possesses some features of a quasi-2D structure. PT0 exhibits

PLQYs of 34 and 48% upon excitation in the blue (at 405 nm) and green (at 485 nm) regions of the spectrum, respectively. To evaluate how moisture affects the PL properties of PT0, PL measurements were also performed on the PT0 NCs in suspension, avoiding contact with the environment during dropcasting. An excitonic peak at ∼430 nm, characteristic of low-dimensional FA $PbBr_5$ perovskites, is now clearly visible (Figure S12). This implies that, after *sec*-butylammonium participates in the formation of a low-dimensional component, traces of water will again deprotonate the ammonium cation by which it escapes the perovskite structure, leaving behind a dominant 3D crystal structure. The post-treated perovskite NCs, on the other hand, exhibit and maintain blue-green emissions after synthesis and dropcasting. As can be seen in Figure 3b, a fundamentally different absorption spectrum as compared to that of PT0 is observed for the treated samples, displaying strong absorption at ∼430 nm and an absorption edge blue-shifted from 528 to 470 nm. The strong peak at 430 nm matches the excitonic absorption peak of the *s*-$BA_2FA_{n-1}Pb_nX_{3n+1}$ structure with $n = 2$,[47] while the absorption edge matches with $n = 4$, indicating a quasi-2D structure (*s*-$BA_2FA_3Pb_4Br_{13}$). This is also consistent with the TEM results, where thin NCs with a thickness of a few nanometers were observed. All three PT1-3 NCs exhibit a sharp emission, peaking at ∼500 nm and revealing a small peak near 430 nm when excited at 395 nm. The blue shift of the emission peak originates from the presence of the low-dimensional perovskite structure. It is anticipated that the quasi-2D structure is stabilized by the presence of NH_4Br, preserving *s*-BA in its protonated form [Scheme 1, left panel (i)]. This assertion can further be supported by the fact that the ionic radius of NH_4^+ (1.54 Å) is smaller than that of protonated butylamine (2.6 Å), which reduces the steric effect, promoting more dense, efficient passivation of the surface.[48] Consequently, the NH_4^+ ions lock the structure of FA $PbBr_5$ upon post-treatment, retaining the blue-green emission, which was not seen in the case of PT0. The PLQY of PT3 directly after synthesis (day 1) reaches 38% at 405 nm excitation. Generally, low-dimensional, blue-emitting perovskites exhibit a comparatively lower PLQY of ∼67% due to enhanced non-radiative recombination processes.[18,49,50] In a time span of 3 days, the post-treated NCs undergo an aging process, during which the emission shifts from blue-green to bright green (Figure S13). In parallel, the absorption peak broadens toward the green spectral region (>505 nm), indicating a more significant contribution of the 3D FA $PbBr_3$ perovskite structure and thereby giving rise to a quasi-2D/3D structure (Figure S13 for additional information). Interestingly, instead of degrading, the post-treated NCs transform into a highly stable system with enhanced PLQYs up to 63 and 85% at 405 and 485 nm excitation, respectively. The increase in the PLQY indicates a decrease in non-radiative decay pathways and a low defect density in the post-treated perovskite NCs. We point out that PT3 remains stable for the longest time, maintaining the highest PLQY. The stability of the PT0 and PT3 NC films is tested by storing the films, both in the glovebox and air (humidity ∼ 66%) and re-measuring them after 21 days. Interestingly, the PLQY of the post-treated NCs dropped only by ∼10%, while PT0 exhibited a drop of ∼40% in a span of 5 days and ∼75% in 21 days, indicating the good stability of PT3 in thin film form under ambient conditions (Figure S14).

An additional test was performed to confirm that the evolution to a more red-shifted PL emission with high PLQY values is associated with the exposure to moisture. For this, as previously stated, a small amount of water [0.2% (v/v)] was added to the PT3 NCs. Thus far, the results above suggest that both the untreated and post-treated NCs initially consist of a coexistence of a low-dimensional structure alongside the conventional 3D FA $PbBr_3$ perovskite structure. When the NCs are exposed to humidity, the low-dimensional component instantly disappears for PT0, while confinement only gradually subsides for PT1-3 by forming a stacked structure, inducing the formation of a quasi-2D/3D structure (Figure S13). The additional stabilization by NH_4Br (absent for PT0) ensures conservation and even improvement of the favorable optical properties after post-treatment. An overview of the complete process of structural rearrangements is given in Scheme 1.

We note three main observations: (i) the addition of water to PT3 yielded large etched steps, a broader size distribution, and fragmented nanocrystallites (Figures 2c,f, and S9). Notably, the crystal structure (XRD) or surface composition (FTIR) was not altered (Figures S15 and S16, respectively). (ii) The emission color instantly turned from blue-green to bright green, yielding a high PLQY of 85 and 95% at 405 and 485 nm excitation, respectively, in the thin film form. (iii) The overall shape of the absorption and PL emission spectra of the water-treated sample resembles that of the spectra of the "aged" PT3 sample after 4 days (Figures 3c and S13b). However, the decrease in the relative contribution of the excitonic peak intensity relative to the total absorbance is likely attributed to the transition of a quasi-2D structure to a more pronounced 3D structure. Additionally, upon water exposure, the NCs self-assemble, forming a stack-like morphology (Figure 2c). This experiment further validates the suggested mechanism that humidity induces the hydrolysis of FABr (in the post-treatment reaction mixture), leading to the formation of NH_4Br, which in turn promotes the stability of the low-dimensional perovskite component. The detailed mechanism responsible for enhanced stability is discussed below.

2.3. PL Red Shift and Role of NH_4Br in Promoting Stability. From the above findings, we postulate that the introduction of NH_4Br at the crystal surface initially forms a passivating layer on the FA $PbBr_5$ surface. Over time, when water (in the form of moisture) interacts with the crystal, it knocks out the constituent ions through etch pit formation (Figure 2e). Generally, such etch pits are deleterious from the stability point of view, facilitating rapid degradation. However, in this case, the presence of NH_4^+ (from free-standing NH_4Br) benefits the crystal structure by compensating the FA vacancies, that is, by partially filling the empty lattice sites formed upon etching. Moreover, the Br-rich environment provided by NH_4Br also assists in defect healing at the surface. This way, the etch pits do not lead to the degradation of NCs,[51,52] but rather allow NH_4^+ ions to penetrate and fill the vacant lattice sites in the structure, which dramatically reduces the defect density [Scheme 1, right panel (ii)]. Generally, the substitution of A-site cations (FA^+, MA^+, or Cs^+) with smaller cations results in lattice contraction, shifting the XRD pattern to a higher 2θ.[53] Similarly, in this case, as the ionic radius of NH_4^+ is substantially smaller than that of FA^+, it causes the lattice to contract. The contraction of the lattice is justified by the XRD pattern, which slightly shifts (by ∼0.1°) to a higher 2θ region on day 3 of the synthesis (Figures S17 and S18). The observed lattice contractions resulting from A -sitecation mixing have been linked to blue-shifted emission and increasing bandgaps.[54] However, in this case, the narrowing

of the bandgap and the transition from blue-green to green emission are attributed to two key factors: (1) the permeation of water molecules in the structure tends to form strong hydrogen bonds with the functional group of the organic moieties and can deprotonate the *sec*-butylammonium cation (Figure S18), thereby transiting the structure from quasi-2D to quasi-2D/3D, without compromising the essential optical performance such as the PLQY; (2) the average particle size of PT3 + H_2O is found to be larger as compared to PT3 (Figure S6c), arising from the stacking of the NCs, which further contributes to the red-shifted emission, as also demonstrated in a previous study.[55] Finally, the enhancement in stability and optoelectronic properties is attributed to the stronger ionic bond between NH_4^+ and Br^- as compared to FA^+ and Br^-, owing to the smaller ionic radius of NH_4^+, thereby exhibiting the "positive aging effect". Alongside, the fragmentation of NCs into small and thin crystallites contributes to the confinement effect in the system (supported by a high E_b, discussed later), boosting the optoelectronic performance of the NCs (Figure S9 and Scheme S2). Overall, it is anticipated that the role of NH_4Br is not merely the passivation of crystal surface, but it also helps in forming a thermodynamically more stable quasi-2D perovskite structure by filling the vacant sites in the structure. An overview of the complete process of structural rearrangements is provided in Scheme 1.

Furthermore, to efficiently study the effect of moisture on the structural evolution of the NCs, an in-situ high-resolution XRD study as a function of time (Figure S18) is performed. This study confirmed the transformation of the PT3 NCs from a quasi-2D structure to a more notable 3D structure when the film is continuously exposed to ambient conditions. Moreover, the XRD pattern shifted slightly to higher 2θ in a course of 5 days, indicating the contraction of lattice. Note that the free-standing NH_4Br remains present even after 5 days, aiding stability in the structure.

To verify if the formation of NH_4Br is necessary for the improved stability and optoelectronic performance, water was also added to the untreated PT0, where no NH_4Br could be formed due to the absence of excess FA. As expected, PT0 degraded soon after adding the water, as demonstrated by its XRD pattern (Figure S19). Also, the PLQY promptly dropped from 48 to 5%. As an additional stability test toward humidity, PT0 and PT3 were dropcasted on a cover slide in ambient conditions. The PT3 sample retained the green color as in suspension, whereas the color of PT0 rapidly changed from green to orange, once again proving enhanced stability for the post-treated NCs (Figure S20). This conclusively demonstrates that the additional NH_4Br in the system leads to higher stability and better optoelectronic performance. It has been previously demonstrated that surface defects give rise to non-radiative recombination centers, leading to shorter charge carrier lifetimes.[56] To gain more insight into the dynamics of the photogenerated carriers, time-resolved PL (TRPL) measurements are performed for all the samples upon 410 nm excitation in the ns and μs regimes, as shown in Figure 4. All TRPL decay profiles fit best to a tri-exponential function, suggesting that the PL decay in the NCs occurs via three main pathways in each regime. For the nanosecond regime, the fast decay components, τ_1 and τ_2 (200 ps−10 ns), are associated with trap-assisted recombination, while the longer component, τ_3 (25−80 ns), is related to unbound exciton recombination.[18] Note that the lifetimes for the post-treated PT1-PT3 NCs

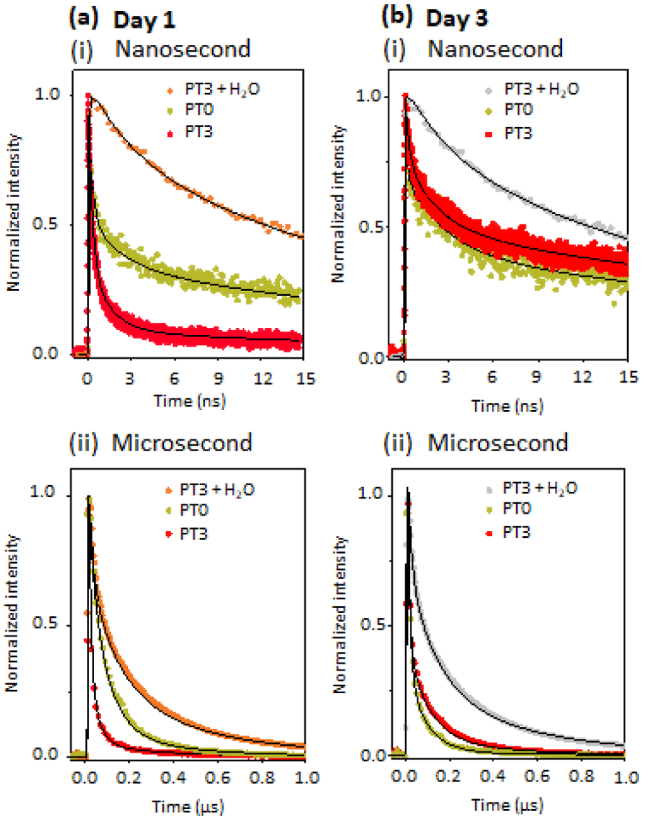

Figure 4. PL decay curves of PT0, PT3, and PT3 + H_2O NCs after synthesis (a, day 1), and after ageing (b, day 3) recorded at the maximum emission wavelengths over the (i) nanosecond and (ii) microsecond timescales (λ_{exc} = 410 nm). Note that the TRPL data obtained for PT3 + H_2O on day 1 is also used for day 3, for comparison with post-treated samples. The different color scheme is used for this purpose.

remain virtually the same, and therefore, we only compare the decays of PT0, PT3, and PT_3+ H_2O to shine light on each stage of the structural evolution (Figure 4). TRPL decays of all the samples were first monitored at 410 nm excitation, and the obtained time constants are provided in the tables in Tables S2 and S3. The experiments are performed in reflection and front-face mode on a NC thin film, minimizing any internal reflection, so a simplified three-exponential model has been used for the decay analysis. TRPL measurements revealed complex emission dynamics, owing to the different proportions of the 2D and 3D perovskite structures before and after treatment. As demonstrated above, on day 1, PT0 and PT3 + H_2O exhibit a bright green emission, indicating a high proportion of 3D NCs, while PT3 displays a blue-green emission, revealing the formation of a quasi-2D structure (Figure S21 for fluorescence microscopy images). The PL decay dynamics on the nanosecond timescale (Figure 4i) are found to correlate perfectly with the dimensionality of the NCs. Generally, as the spatial dimension decreases, the surface-to-volume ratio increases, resulting in a relatively higher content of surface defects.[57,58] Directly after synthesis (Figure 4a, day 1), the TRPL decay for post-treated samples is largely dominated by the fast decay components, τ_1 and τ_2, indicating trap-assisted recombination on or near the surface. Impor-tantly, for PT0, the slow-decay component, τ_3, possesses the highest relative amplitude, revealing radiative exciton recombi-nation in the bulk, which is possible by the predominant 3D

structure of PT0.[59,60] As can be seen in Figure 4b, on day 3, the structural rearrangement in the post-treated samples induces an overall reduction in the amplitudes of the fast trap-assisted recombination, pointing towards the reduction of surface traps. Note that the water-treated PT3 instantly undergoes a moisture-induced structural rearrangement, accompanied by a PL shift from blue-green to green. Since this structure is equivalent to that of PT3 on day 3, the TRPL of PT3 + H_2O on day 1 is compared to that of the PT3 on day 3 in Figure 4b. Furthermore, the lifetime and amplitude of the τ_3 component in PT3 increased by three and five fold, respectively. This provides strong evidence for a reduced number of surface charge traps when the material is exposed to air humidity.[61] The enhancement in this long lifetime component is attributed to a collection of factors: (1) a more stable structure is formed upon the partial substitution of FA^+ with NH_4^+, resulting in stronger interaction with the halides of the octahedral units. (2) Halide-rich surface provided by NH_4Br. (3) Last, the transition from a quasi-2D to a quasi-2D/3D structure results in emission in a relatively smaller bandgap, which is effectively stabilized by the presence of free NH_4Br. These findings are also consistent with the TRPL decay of the water-treated PT3 (Figure 4a). In contrast, after 3 days, the τ_3 value for PT0 dropped by 64% of its initial value on day 1, implying the degradation of the untreated sample with time (Figure 4b, Table S2). Additionally, the decay dynamics were monitored in the green spectral region upon 480 nm excitation. As expected, the amplitudes for τ_2 and τ_3 are very low for the post-treated NCs on Day 1, as the absorption and emission are mainly governed by the blue emitting 2D structure (Table S3).

To gain more insight into the longer timescale, PL decays in the μs regime were recorded (Figure 4ii and Table S2). Tri-exponential fits were applied to the experimental data to quantify the carrier dynamics. In this case, the short components, τ_4 and τ_5, are assigned to unbound exciton recombination occurring in the quasi-2D and in the bulk 3D structures and are roughly comparable to the τ_3 of the data recorded in the ns regime. The long-lived component, τ_6, corresponds to free-charge carrier recombination. On day 1 (Figure 4a), the longest decay is observed for PT3 + H_2O, attributed to the dominant presence of 3D structure. Additionally, the presence of free NH_4Br assists in stabilizing the structure by filling the vacant FA -sites formed upon etching. Notably, on day 3 (Figure 4b), PT0 exhibits a substantial decline in the amplitude of the longest component and a rise in that of the shortest one, which is typical for a system including more defects. On the other hand, the overall lifetime of PT3 increases in the following days after synthesis, illustrating an enhancement of radiative recombination within the material and hinting at efficient passivation of the surface. These findings are consistent with the lifetime parameters of PT3 + H_2O on day 1 (Figure 4a,b).

Next, the temperature-dependent PL intensity (4.2–300 K) is carefully evaluated for PT0, PT3, and PT3 + H_2O directly after synthesis (day 1) and on day 3. These data allow to quantifying the E_b of the $FAPbBr_3$ NCs as a direct measure for the structural confinement. In Figure 5a–c, the PL spectra normalized to the PL maximum at selected T_s between 4.2 and 300 K are shown for PT0, PT3, and PT3 + H_2O on day 1 and day 3 (for raw data, see Supporting Information Figure S22). The spectra are shifted vertically for clarity. The PL peak is blue-shifted as a function of temperature, which is typical for

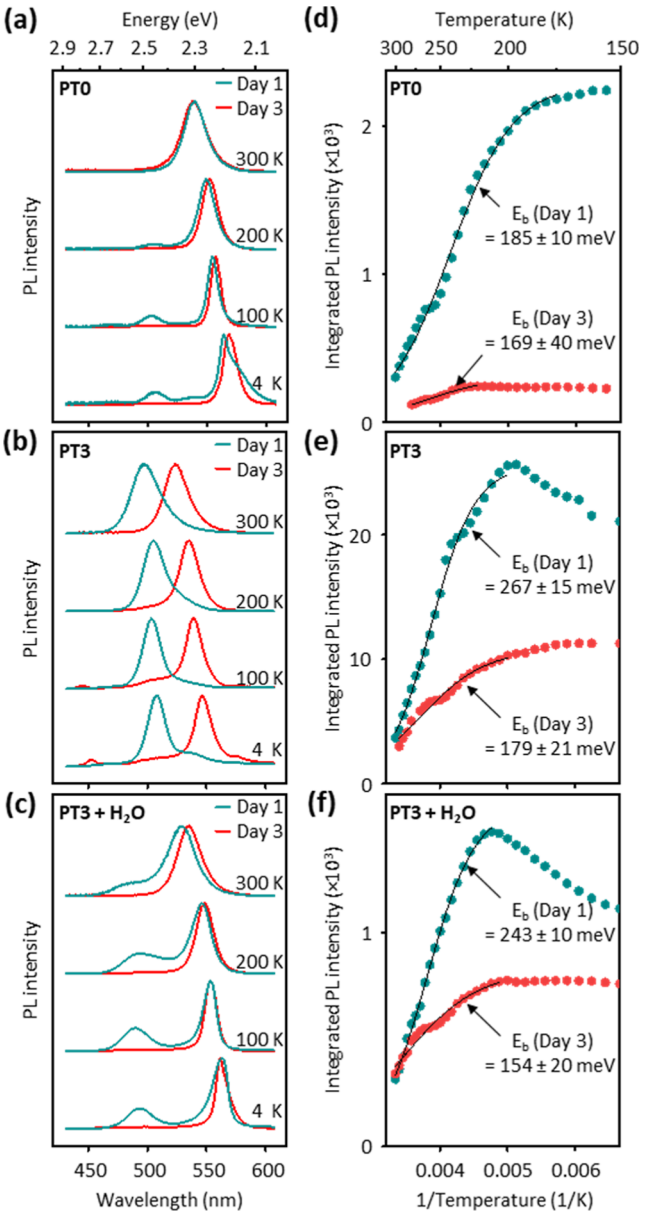

Figure 5. Temperature evolution of the PL spectra for PT0, PT3, and PT3 + H_2O NCs on day 1 and day 3. (a–c) Selected PL spectra normalized to their PL maximum at different temperatures for (a) PT0, (b) PT3, and PT3 + H_2O on day 1 (green curves) and day 3 (red curves). The spectra are shifted vertically for clarity. (d–f) Arrhenius plots of the integrated PL intensity for (d) PT0, (e) PT3, and (f) PT3 + H_2O on day 1 (green circles) and day 3 (red squares). The solid curves represent the fits based on eq 1 to extract the E_b for each system.

this class of perovskites.[62] Abrupt changes in the PL peak position are observed for all three samples and are attributed to structural phase transitions in $FAPbBr_3$[63] (Figure S23d–f). The phase transition temperatures are not altered upon post-treatment; hence, no changes in the bulk crystal structure have been induced. For PT0 and PT3 + H_2O, two peaks in the PL spectra around 563 nm (2.2 eV) and 506 nm (2.45 eV) are observed, with the one at 563 nm (2.2 eV) being the fundamental PL peak for these materials, which we analyze and discuss hereafter (Figure 5a–c).

Looking at the PL peak maxima (eV) extracted from Gaussian fits to the PL spectra at each temperature on day 1

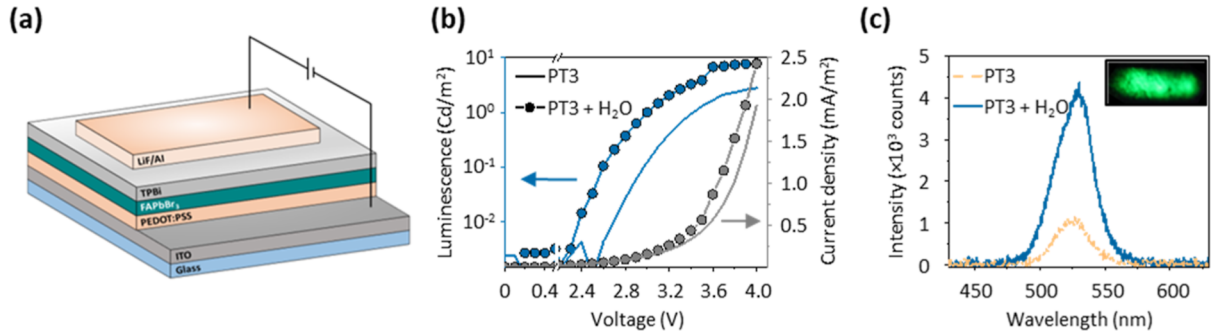

Figure 6. (a) Device structure, (b) $I-V$ response curve, and (c) EL spectra of hybrid multilayer devices up to 4.6 voltage supply for PT3 and PT3 + H_2O.

and day 3, a negligible shift is observed for PT0 and PT3 + H_2O (Figure S23a−c). However, a relatively large shift from high energy (E = 2.45 eV at 300 K) to lower energy (E = 2.35 eV at 300 K) is detected for PT3 over this time span. We attribute this shift to the gradual transition from a quasi-2D to a quasi-2D/3D structure over 48 h, as also found in the time-resolved XRD as well (Figure S18). In Figure 5d−f, the integrated PL intensity extracted from Gaussian fits versus inverse temperature is illustrated. From day 1 to day 3, a 50% drop in the intensity of the PL peak maximum occurs for PT0, while only a 20% decrease in intensity is observed for PT3 and PT3 + H_2O, confirming an induced stability through post-treatment (see Figure 5d−f). We evaluated the E_b of each system by modeling the temperature dependence of the PL intensity in the cubic phase by the Arrhenius equation

$$I(T) = I_0/(1 + Ae^{-E_b/k_BT}) \quad (1)$$

as illustrated in Figure 5d−f, where I_0 and A are constants and k_B is the Boltzmann constant. E_b extracted for PT0 is around 180 meV. For PT3 and PT3 + H_2O, the E_b on day 1 increases to 270 and 250 meV, respectively, due to the confinement imposed by the quasi-2D structure. On day 3, this value shifts back to 154 meV for PT3 + H_2O and to 180 meV for PT3, similar to PT0 on day 1, due to structural rearrangement to a stabilized quasi-2D/3D system.

2.4. Device Performance. The high PLQY values and enhanced stability of the post-treated NCs make them very promising for optical applications, in particular for LEDs. To investigate their performance in devices, we fabricated LED devices using PT3 (day 3) and PT3 + H_2O NCs as the electroluminescent (EL) layer. The LEDs exhibit following configuration: ITO/PEDOT/PSS/perovskite//TPBi//LiF/Al, where PEDOT/PSS and TPBi refer to poly(3,4-ethylenedioxythiophene) polystyrene sulfonate and 2,2,2″-(1,3,5-benzinetriyl)-tris(1-phenyl-1-*H*-benzimidazole), respectively (Figure 6a). The design and composition of this device are in agreement with the conduction and valence bands of the samples, which are situated around ∼3.4 and 5.6 eV, respectively.[64] Note that TPBi is added to inhibit the direct interaction between the Al metal and the perovskite material, which in many cases degrades the perovskite.[53] For PT3, a typical diode characteristic is observed with a turn-on voltage of 2.5 V. The luminescence versus voltage is plotted in Figure 6b, demonstrating a value of 2 Cd/m^2 at 4 V.

To gain further insight into the optoelectronic properties of the device, the EL spectra were recorded at 4.6 V. In the case of PT3, the EL signal exhibits a narrow peak at ∼525 nm (2.36 eV, fwhm 1100 cm^{-1}), which is red-shifted as compared to its corresponding PL peak at ∼506 nm (2.54 eV, fwhm 1100 cm^{-1}) (Figures S13 and S24). This issue has been widely observed in PeLEDs and is ascribed to the carrier trapping at the grain boundaries, different trap states in the crystal structure,[65] or the interfaces between two different layers.[66] Generally, in the LED configuration, the injected charge carriers are prone to undergo a trapping process by these electron−hole recombination centers, with energy levels residing within the bandgap. Thereby, the relative energy difference upon radiative recombination is reduced, con-sequently red-shifting the EL spectra. Furthermore, one of the major obstacles in having high efficiencies in perovskite-based LEDs is the presence of water; however, the role of water on the EL properties was also investigated, employing the same device structure for the PT3 + H_2O NCs. The PL and EL spectra exhibited nearly the same maxima [∼530 nm (2.33 eV)], indicating emission from the same electronic excited state, thereby suggesting the suppression of carrier trapping at the defect sites. However, the broader fwhm (increasing from 810 to 1500 cm^{-1}) under a forward voltage may relate to the heterogeneous morphology or the defects generated at the interfaces in this proof-of-concept LED device. A closer look at the EL spectra of both the samples indicates that the EL mechanism remains unchanged, as it is proven by the CIE coordinates (0.17, 0.74) (Figure S25). However, the device shows a lower turn-on voltage of 2.3 V and a four times higher EL at the same voltage (8 Cd/m^2) as compared to PT3. The enhanced LED efficiency is supported by the three-fold increase of the EQE for the device with PT3 + H_2O. It should be noted that the still relatively low EQE found here can be attributed to the large size of the NCs, which can lead to their aggregation in solution and subsequent poor coverage of the substrates. Nevertheless, this proof-of-concept study confirms that water can actually improve perovskite-based LED device performance as its presence is not necessarily detrimental for the material quality. We have summarized the most relevant PLQY and LED-device figures from a handful of literature reports on water-exposed perovskite NCs (mainly $CsPbBr_3$ and MA $PbBr_3$-based NCs and double perovskite nanostructures) in Table S4. Based on these findings, there is plenty of room for improving the device performance by downsizing the NCs and fine-tuning the film quality and device architecture, which have not been optimized as part of this study.

3. CONCLUSIONS

This study shows that water is not always a threat to perovskite-based devices, but that it can positively affect the

stability and optoelectronic performance when the device is composed of rationally engineered perovskite materials. A facile post-treatment strategy is reported which allows achieving high-quality, water-compatible $FAPbBr_3$ NCs. A combination of advanced structural and optical characterization techniques proves that moisture-induced hydrolysis of the excess of FABr, applied during post-treatment, results in a surface-passivating layer of NH_4Br, responsible for the improved stability. As such, the stability and crystalline quality of the perovskite NCs are substantially enhanced, while yielding a high PLQY of 95% after deposition as a device-ready NC thin film. We also demonstrate the role of water in promoting localized exfoliation of the post-treated NCs, which in turn leads to the partial intercalation of NH_4^+, boosting the stability. These new findings offer opportunities toward commercial application of perovskites in moisture-stable optoelectronics.

4. METHODS

4.1. Experimental Procedure. For the synthesis of PT0 FA $PbBr_3$ NCs, a precursor solution consisting of 1 mmol of $PbBr_2$ and 1 mmol of FABr dissolved in 2.5 mL of DMF was prepared. From this, 0.25 mL of the precursor solution was injected slowly into a vigorously stirring toluene solution, containing *sec*-butylamine (*s*-BA) and oleic acid (OAc) as capping ligands. To ensure colloidal stability, the molar amounts of OAc and *s*-BA were fixed to 0.5 and 0.8 mmol, respectively. After injection, highly luminescent NCs were rapidly formed, and to further promote the precipitation, an extra volume of toluene was subsequently added to the suspension. The resulting NCs were centrifuged at 3000 rpm for 4 min and washed with toluene to remove the excess capping agents and unreacted precursor. Finally, they were redispersed in toluene, forming a stable colloidal solution. Next, for the post-treatment step, 1, 2, and 3 molar equivalents of FA Br, being 0.02, 0.04, and 0.06 mmol, were dissolved in hexane containing OAc and oleylamine (OAm). The mixtures were sonicated at 60 °C for 3−4 h, which did not form a clear solution but a suspension. Later, the PT0 NCs were shortly sonicated in this mixture and further centrifuged at 3000 rpm for 4 min. The resulting NCs were redispersed in hexane, yielding blue-green emission under a UV lamp. For preparing PT3 + H_2O, 2 μL of water was added to the PT3 NCs, and the mixture was sonicated shortly. Note that the added amount of water and the sonication time both play a significant role. The perovskites' suspension changes color from light green to bright green to yellow when too much water is added or when treated for a longer time, deteriorating the optical properties. Please consult the Supporting Information for a schematic representation of the synthesis procedure (Figure S26).

4.2. Instrumental Analysis. *4.2.1. Scanning Electron Microscopy.* Morphology and composition analysis were studied using an FEI Quanta FEG-250 environmental scanning electron microscope at 10 KV, equipped with an energy-dispersive spectrometer. The NC suspension was dropcasted on a silicon chip prior to the measurement.

4.2.2. X-ray Diffraction. A Malvern PANalytical Empyrean diffractometer using a Debye−Scherrer transmission geometry equipped with a PIXcel3D solid-state detector using a Cu anode. Data were collected on the thin films in the range of 1−45° with a step size of 0.0131° and 79 s as counting time.

The indexing of the powder pattern in free objects for crystallography (FOX)[67] indicates the presence of a mixture of two cubic phases, see Figures 2a and S2. Rietveld refinement in FullProf[68] proves the correspondence of the minor phase (~40 wt % according to the refinement) with slightly broader peaks to the typical cubic structure of FA $PbBr_3$ [$Pm\bar{3}m$ a = 6.0179(2) Å],[29] while the second one with sharp peaks (marked with #) is assigned to the cubic ammonium bromide (NH_4Br) structure [$Pm\bar{3}m$, a = 4.0620(1) Å],[69] initially found by the unit cell parameters in Crystallography Open Database (COD).[70]

4.2.3. Grazing Incidence X-ray Diffraction. Thin films were characterized with a Malvern PANalytical Empyrean diffractometer equipped with a PIXcel3D solid-state detector using a Cu anode. Before each measurement, an iterative scheme was employed to optimize the sample height and tilt. GIXRD patterns were recorded in reflection geometry with an incident angle ω = 0.2°. The 2θ range scanned was 1−15°, using a step size of 0.053°/s and a counting time of 1000 s per step. A fixed antiscatter slit of 1/16° fixed was used on the source side to limit the beam divergence.

4.2.4. X-ray Photoelectron Spectroscopy. XPS data were recorded using a K-alpha Thermo spectrometer with an Al Kα radiation at 1486.68 eV.

4.2.5. Fourier-Transform Infrared Spectroscopy. Attenuated total reflection−FTIR (ATR−FTIR) spectra were recorded on a Varian 670 FTIR spectrometer equipped with a VeeMAXTM III accessory (PikeTech).

4.2.6. Scanning Transmission Electron Microscopy. High-resolution HAADF−STEM images were acquired with a probe-corrected cubed Thermo Fisher Scientific Themis Z microscope operating at 300 kV with a probe semi-convergence angle of 20.5 mrad.

4.2.7. UV−Vis Diffuse Reflectance Spectroscopy. Diffuse reflectance spectra (DRS) were recorded on a PerkinElmer Lambda 950 UV−vis−NIR spectrophotometer with the 150 mm integrating sphere accessory in the wavelength range between 300 and 600 nm. The diffuse reflectance (R) data were converted to $F(R)$ using the Kubelka−Munk function: $F(R) = (1 - R)^2/(2R)$.

4.2.8. Emission and Excitation Spectroscopy. Excitation and emission spectra were recorded on an Edinburgh Instruments FLS 980 spectrofluorimeter. Samples were measured in front-face mode as thin films created by dropcasting a suspension onto a glass slide that fitted into the Edinburgh solids accessory.

4.2.9. PL Quantum Yield. Quantum yield measurements were performed on a Horiba Fluorolog 3.22 spectrofluorimeter with an F-3029 integrating sphere accessory fitted with a sample holder to accommodate thin film samples drop-casted on a glass slide.

4.2.10. PL Lifetime Spectroscopy. PL lifetimes at a 410 nm excitation wavelength and 58 J/cm^2 fluence were recorded. The fluorescence decay times at the nanosecond time scale were determined by the TC-SPC technique. The fluorescence was spectrally resolved by a monochromator (Sciencetech 9030, 100 nm focal length, wave-length accuracy 0.3 nm) and detected by a microchannel plate photomultiplier tube (MCP-PMT, R3809U-51, Hamamatsu). A time-correlated single photon timing PC module (SPC 830, Becker & Hickl) was used to obtain the fluorescence decay histogram in 4096 channels. The decays were recorded with 10,000 counts in the peak channel in time windows of 17 ns, corresponding to 4.25 ps per channel, and analyzed individually with a time-resolved fluorescence analysis (TRFA) software based on iterative reconvolution of the data with the instrumental response function (IRF). The fwhm of the IRF was typically in the order of 42 ps.

Nanosecond to millisecond time-resolved luminescence: a 410 nm laser pulse (8 ns, 10 Hz) generated by a system consisting of a pulsed Nd/YAG laser (Quanta-Ray INDI-40, Spectra Physics) was used to excite the samples. The excitation light was focused on the sample by a 150 mm focal length lens, and a small part of this light was sent to a fast photodiode to generate a trigger signal. Right angle configuration between excitation and light collection paths was used, and the luminescence was collected, filtered, and focused on the entrance slit of a 30 cm focal length monochromator. A homemade Labview-based software was used to control and trigger the instruments, read, average, and store the transient data.

4.2.11. Low-Temperature PL Measurement. For low-temperature PL measurements, the sample was drop-casted on a quartz plate and mounted on an insert in a He flow cryostat, in which the temperature can be varied from 4.2 to 300 K. We used a solid-state laser Thorlabs M365LP1 with driver DC2200 operating at 365 nm for excitation. The laser was coupled to a 550 μm core optical fiber. The PL spectra were collected through 11 core optical fibers of 200 μm diameter that are surrounding the excitation fiber. The detection fibers are coupled

to a LOT-QD Shamrock F/4 spectrometer with an electron multiplying charge-coupled detector (EMCCD) iXon DV887. The PL spectra were collected at 5 K increment.

4.2.12. Device Fabrication and Characterization. The glass/ITO substrates were washed in an ultrasonic bath with soap water, deionized water, acetone, and isopropanol for 10 min, respectively. After drying with nitrogen, they were treated with UV-ozone for 15 min. Then, PEDOT/PSS dispersion (Clevios P VP AI 4083) was spin-coated on the pre-cleaned ITO substrates at 4000 rpm for 60 s, followed by thermal annealing at 110 °C for 10 min. After that, the perovskite films were deposited in a N_2-filled glove box by spincoating a 20 mg/mL nanocrystal solution in hexane at 1000 rpm. The devices were finished by evaporation of 40 nm TPBi, 1.2 nm LiF, and 100 nm Al layers on top of the perovskite films sequentially. The device area was 0.125 cm^2, with dimensions of 2.5 mm × 5 mm. A Thorlabs integrating sphere (IS236A-4), coupled with a calibrated silicon photodiode (SM05PD1B), and a flame spectrometer from Ocean Optics were used to measure the EL intensity and the emission spectrum. The response of the photodiode was calibrated together with the integrating sphere by Thorlabs. The *J*−*V* characteristics were measured by an Agilent 4156C Semiconductor Parameter Analyzer, which also records the corresponding light-induced photodiode current at the same time.

■ ASSOCIATED CONTENT

Supporting Information

Additional information on results, including the reaction mechanism of the hydrolysis of FABr; XRD peak fitting of PT3; XRD patterns of post-treated suspension and mixture of FABr + OAm + H_2O, revealing the NH_4Br phase; XRD pattern of post-treated NCs with different amounts of NH_4Br and formamide; GIXRD pattern of PT3; FTIR spectra of ligands employed in the synthesis; peak analysis of XPS spectra; size distribution of PT0, PT3, and PT3 + H_2O NCs; HAADF-STEM image of PT0 NCs and its corresponding FFT pattern; STEM images of PT3 NCs; STEM images of PT3 + H_2O; scheme depicting the role of moisture in assisting dissolution−recrystallization of NCs and localized exfoliation; diffraction pattern of PT3; HAADF image of PT3 + H_2O, shielded by a sphere and elemental mapping obtained from EDX; PL and absorption spectra of PT0 in suspension; PL and absorption spectra of PT1-3 on days 3 and 4; PL emission spectra of PT0 and PT3 recorded on day 1 and day 21 on same films, when stored in air (humidity 66%); XRD and FTIR results of PT3 + H_2O; XRD pattern of PT3, recorded on day 1 and 3, depicting the shift to a higher angle; XRD data of PT3 as a function of time; XRD of PT0 + H_2O; thin-film images of sample when dropcast in air, displaying stability; fluorescence microscopy images of PT3 and of PT3 + H_2O on day 1; PL decay values of PT0, PT3, and PT3 + H_2O obtained from the nanosecond setup on days 1 and 3 at 405 nm excitation; recombination lifetimes of PT0 and PT3 obtained from the nanosecond setup on days 1 and 3 at 480 nm excitation; PL mapping upon cooling for PT0, PT3, and PT3 + H_2O; PL temperature evolution of the PL spectra for PT0, PT3, and PT3 + H_2O on days 1 and 3; CIE coordinates for PT3 and PT3 + H_2O; and design of the synthesis protocol (PDF)

■ AUTHOR INFORMATION

Corresponding Author

Elke Debroye − *Department of Chemistry, KU Leuven, 3001 Leuven, Belgium;* orcid.org/0000-0003-1087-4759; Email: elke.debroye@kuleuven.be

Authors

Harshita Bhatia − *Department of Chemistry, KU Leuven, 3001 Leuven, Belgium*

Cristina Martin − *Department of Chemistry, KU Leuven, 3001 Leuven, Belgium; Department of Physical Chemistry, Faculty of Pharmacy, University of Castilla-La Mancha, 02071 Albacete, Spain;* orcid.org/0000-0002-7588-8759

Masoumeh Keshavarz − *Department of Chemistry, KU Leuven, 3001 Leuven, Belgium;* orcid.org/0000-0003-3685-6778

Iurii Dovgaliuk − *Institut des Matériaux Poreux de Paris, Ecole Normale Supérieure, ESPCI Paris, CNRS, PSL Université, 75005 Paris, France*

Nadine J. Schrenker − *Electron Microscopy for Materials Science (EMAT) and NANOlab Center of Excellence, University of Antwerp, B-2020 Wilrijk, Belgium*

Martin Ottesen − *Department of Chemistry and iNANO, Aarhus University, 8000 Aarhus C, Denmark*

Weiming Qiu − *Department of Chemistry, KU Leuven, 3001 Leuven, Belgium*

Eduard Fron − *Department of Chemistry, KU Leuven, 3001 Leuven, Belgium;* orcid.org/0000-0003-2260-0798

Martin Bremholm − *Department of Chemistry and iNANO, Aarhus University, 8000 Aarhus C, Denmark;* orcid.org/0000-0003-3634-7412

Joris Van de Vondel − *Quantum Solid-State Physics (QSP), Department of Physics and Astronomy, KU Leuven, Leuven 3001, Belgium;* orcid.org/0000-0001-6894-7258

Sara Bals − *Electron Microscopy for Materials Science (EMAT) and NANOlab Center of Excellence, University of Antwerp, B-2020 Wilrijk, Belgium;* orcid.org/0000-0002-4249-8017

Maarten B.J. Roeffaers − *cMACS, Department of Microbial and Molecular Systems, KU Leuven, 3001 Leuven, Belgium;* orcid.org/0000-0001-6582-6514

Johan Hofkens − *Department of Chemistry, KU Leuven, 3001 Leuven, Belgium;* orcid.org/0000-0002-9101-0567

Notes

The authors declare no competing financial interest.

■ ACKNOWLEDGMENTS

H.B. would like to express her sincere gratitude to Dr. Peter Erk (formerly BASF SE, Germany) for very insightful discussions. The authors acknowledge financial support from the Research Foundation-Flanders (FWO grant numbers S002019N, 1514220N, G.0B39.15, G.0B49.15, G098319N, and ZW15_09-GOH6316), the KU Leuven Research Fund (C14/19/079, iBOF-21-085 PERSIST, and STG/21/010), the Flemish government through long-term structural funding Methusalem (CASAS2, Meth/15/04), the Hercules Foundation (HER/11/14), and the ERC through the Marie Curie ITN iSwitch Ph.D. fellowship to H.B. (grant number 642196). C.M. acknowledges the financial support from grants

PID2021-128761OA-C22 funded by MCIN/AEI/10.13039/501100011033 by the "European Union" and SBPLY/21/180501/000127 funded by JCCM and by the EU through "Fondo Europeo de Desarollo Regional" (FEDER). Martin Bremholm and Martin Ottesen acknowledge funding from the Danish Council for Independent Research, Natural Sciences, under the Sapere Aude program (grant no. 7027-00077B) and VILLUM FONDEN through the Centre of Excellence for Dirac Materials (grant no. 11744). Affiliation with the Center for Integrated Materials Research (iMAT) at Aarhus University is gratefully acknowledged.-N.J.S. acknowledges financial support from the research foundation Flanders (FWO) through a postdoctoral fellowship (FWO grant no. 1238622N). S.B. acknowledges financial support from the European Commission by the ERC Consolidator grant REALNANO (no. 815128).

REFERENCES

(1) Yuan, M.; Quan, L. N.; Comin, R.; Walters, G.; Sabatini, R.; Voznyy, O.; Hoogland, S.; Zhao, Y.; Beauregard, E. M.; Kanjanaboos, P.; Lu, Z.; Kim, D. H.; Sargent, E. H. Perovskite Energy Funnels for Efficient Light-Emitting Diodes. *Nat. Nanotechnol.* **2016**, *11*, 872−877.

(2) Dey, A.; Ye, J.; De, A.; Debroye, E.; Ha, S. K.; Bladt, E.; Kshirsagar, A. S.; Wang, Z.; Yin, J.; Wang, Y.; Quan, L. N.; Yan, F.; Gao, M.; Li, X.; Shamsi, J.; Debnath, T.; Cao, M.; Scheel, M. A.; Kumar, S.; Steele, J. A.; Gerhard, M.; Chouhan, L.; Xu, K.; Wu, X.; Li, Y.; Zhang, Y.; Dutta, A.; Han, C.; Vincon, I.; Rogach, A. L.; Nag, A.; Samanta, A.; Korgel, B. A.; Shih, C.-J.; Gamelin, D. R.; Son, D. H.; Zeng, H.; Zhong, H.; Sun, H.; Demir, H. V.; Scheblykin, I. G.; Mora-Seró, I.; Stolarczyk, J. K.; Zhang, J. Z.; Feldmann, J.; Hofkens, J.; Luther, J. M.; Pérez-Prieto, J.; Li, L.; Manna, L.; Bodnarchuk, M. I.; Kovalenko, M. V.; Roeffaers, M. B. J.; Pradhan, N.; Mohammed, O. F.; Bakr, O. M.; Yang, P.; Müller-Buschbaum, P.; Kamat, P. V.; Bao, Q.; Zhang, Q.; Krahne, R.; Galian, R. E.; Stranks, S. D.; Bals, S.; Biju, V.; Tisdale, W. A.; Yan, Y.; Hoye, R. L. Z.; Polavarapu, L. State of the Art and Prospects for Halide Perovskite Nanocrystals. *ACS Nano* **2021**, *15*, 10775−10981.

(3) Liu, X.-K.; Xu, W.; Bai, S.; Jin, Y.; Wang, J.; Friend, R. H.; Gao, F. Metal Halide Perovskites for Light-Emitting Diodes. *Nat. Mater.* **2021**, *20*, 10−21.

(4) Krishna, A.; Gottis, S.; Nazeeruddin, M. K.; Sauvage, F. Mixed Dimensional 2D/3D Hybrid Perovskite Absorbers: The Future of Perovskite Solar Cells? *Adv. Funct. Mater.* **2019**, *29*, 1806482.

(5) Bhatia, H.; Ghosh, B.; Debroye, E. Colloidal FAPbBr 3 Perovskite Nanocrystals for Light Emission: What's Going On? *J. Mater. Chem. C* **2022**, *10*, 13437−13461.

(6) Chen, Y.; Sun, Y.; Peng, J.; Tang, J.; Zheng, K.; Liang, Z. 2D Ruddlesden−Popper Perovskites for Optoelectronics. *Adv. Mater.* **2018**, *30*, 1703487.

(7) Zhu, X.; Xu, Z.; Zuo, S.; Feng, J.; Wang, Z.; Zhang, X.; Zhao, K.; Zhang, J.; Liu, H.; Priya, S.; Liu, S. F.; Yang, D. Vapor-Fumigation for Record Efficiency Two-Dimensional Perovskite Solar Cells with Superior Stability. *Energy Environ. Sci.* **2018**, *11*, 3349−3357.

(8) Zhang, Y.; Keshavarz, M.; Debroye, E.; Fron, E.; Rodríguez González, M. C. R.; Naumenko, D.; Amenitsch, H.; Van de Vondel, J.; De Feyter, S. D.; Heremans, P.; Roeffaers, M. B. J.; Qiu, W.; Pradhan, B.; Hofkens, J. Two-Dimensional Perovskites with Alternating Cations in the Interlayer Space for Stable Light-Emitting Diodes. *Nanophotonics* **2020**, *10*, 2145−2156.

(9) Ye, J.; Byranvand, M. M.; Martínez, C. O.; Hoye, R. L. Z.; Saliba, M.; Polavarapu, L. Defect Passivation in Lead-Halide Perovskite Nanocrystals and Thin Films: Toward Efficient LEDs and Solar Cells. *Angew. Chem.* **2021**, *133*, 21804−21828.

(10) Zheng, X.; Chen, B.; Dai, J.; Fang, Y.; Bai, Y.; Lin, Y.; Wei, H.; Zeng, X. C.; Huang, J. Defect Passivation in Hybrid Perovskite Solar Cells Using Quaternary Ammonium Halide Anions and Cations. *Nat. Energy* **2017**, *2*, 17102.

(11) Ahmed, T.; Seth, S.; Samanta, A. Boosting the Photoluminescence of $CsPbX_3$ (X = Cl, Br, I) Perovskite Nanocrystals Covering a Wide Wavelength Range by Postsynthetic Treatment with Tetrafluoroborate Salts. *Chem. Mater.* **2018**, *30*, 3633−3637.

(12) Ahmed, G. H.; Yin, J.; Bose, R.; Sinatra, L.; Alarousu, E.; Yengel, E.; AlYami, N. M.; Saidaminov, M. I.; Zhang, Y.; Hedhili, M. N.; Bakr, O. M.; Brédas, J.-L.; Mohammed, O. F. Pyridine-Induced Dimensionality Change in Hybrid Perovskite Nanocrystals. *Chem. Mater.* **2017**, *29*, 4393−4400.

(13) Li, H.; Qian, Y.; Xing, X.; Zhu, J.; Huang, X.; Jing, Q.; Zhang, W.; Zhang, C.; Lu, Z. Enhancing Luminescence and Photostability of $CsPbBr_3$ Nanocrystals via Surface Passivation with Silver Complex. *J. Phys. Chem. C* **2018**, *122*, 12994−13000.

(14) Liu, M.; Wan, Q.; Wang, H.; Carulli, F.; Sun, X.; Zheng, W.; Kong, L.; Zhang, Q.; Zhang, C.; Zhang, Q.; Brovelli, S.; Li, L. Suppression of Temperature Quenching in Perovskite Nanocrystals for Efficient and Thermally Stable Light-Emitting Diodes. *Nat. Photonics* **2021**, *15*, 379−385.

(15) Kim, Y.-H.; Kim, S.; Kakekhani, A.; Park, J.; Park, J.; Lee, Y.-H.; Xu, H.; Nagane, S.; Wexler, R. B.; Kim, D.-H.; Jo, S. H.; Martínez-Sarti, L.; Tan, P.; Sadhanala, A.; Park, G.-S.; Kim, Y.-W.; Hu, B.; Bolink, H. J.; Yoo, S.; Friend, R. H.; Rappe, A. M.; Lee, T.-W. Comprehensive Defect Suppression in Perovskite Nanocrystals for High-Efficiency Light-Emitting Diodes. *Nat. Photonics* **2021**, *15*, 148−155.

(16) Ambrosio, F.; Meggiolaro, D.; Mosconi, E.; De Angelis, F. D. Charge Localization and Trapping at Surfaces in Lead-Iodide Perovskites: The Role of Polarons and Defects. *J. Mater. Chem. A* **2020**, *8*, 6882−6892.

(17) Yang, Y.; Yang, M.; Moore, D. T.; Yan, Y.; Miller, E. M.; Zhu, K.; Beard, M. C. Top and Bottom Surfaces Limit Carrier Lifetime in Lead Iodide Perovskite Films. *Nat. Energy* **2017**, *2*, 16207.

(18) Bhatia, H.; Steele, J. A.; Martin, C.; Keshavarz, M.; Solis-Fernandez, G.; Yuan, H.; Fleury, G.; Huang, H.; Dovgaliuk, I.; Chernyshov, D.; Hendrix, J.; Roeffaers, M. B. J.; Hofkens, J.; Debroye, E. Single-Step Synthesis of Dual Phase Bright Blue-Green Emitting Lead Halide Perovskite Nanocrystal Thin Films. *Chem. Mater.* **2019**, *31*, 6824−6832.

(19) Zhang, L.; Yuan, F.; Jiao, B.; Dong, H.; Li, J.; Wu, Z. Exploiting a Multiphase Pure Formamidinium Lead Perovskite for Efficient Green-Light-Emitting Diodes. *ACS Appl. Mater. Interfaces* **2021**, *13*, 23067−23073.

(20) Ghosh, S.; Nim, G. K.; Bansal, P.; Kar, P. Investigating the Property of Water Driven Lead-Free Stable Inorganic Halide Double Perovskites. *J. Colloid Interface Sci.* **2021**, *582*, 1223−1230.

(21) Debroye, E.; Yuan, H.; Bladt, E.; Baekelant, W.; Van der Auweraer, M.; Hofkens, J.; Bals, S.; Roeffaers, M. B. J. Facile Morphology-Controlled Synthesis of Organolead Iodide Perovskite Nanocrystals Using Binary Capping Agents. *ChemNanoMat* **2017**, *3*, 223−227.

(22) Eperon, G. E.; Habisreutinger, S. N.; Leijtens, T.; Bruijnaers, B. J.; van Franeker, J. J.; deQuilettes, D. W.; Pathak, S.; Sutton, R. J.; Grancini, G.; Ginger, D. S.; Janssen, R. A. J.; Petrozza, A.; Snaith, H. J. The Importance of Moisture in Hybrid Lead Halide Perovskite Thin Film Fabrication. *ACS Nano* **2015**, *9*, 9380−9393.

(23) Liu, K.-K.; Liu, Q.; Yang, D.-W.; Liang, Y.-C.; Sui, L.-Z.; Wei, J.-Y.; Xue, G.-W.; Zhao, W.-B.; Wu, X.-Y.; Dong, L.; Shan, C.-X. Water-Induced $MAPbBr_3$ @PbBr(OH) with Enhanced Luminescence and Stability. *Light: Sci. Appl.* **2020**, *9*, 44.

(24) Turedi, B.; Lee, K. J.; Dursun, I.; Alamer, B.; Wu, Z.; Alarousu, E.; Mohammed, O. F.; Cho, N.; Bakr, O. M. Water-Induced Dimensionality Reduction in Metal-Halide Perovskites. *J. Phys. Chem. C* **2018**, *122*, 14128−14134.

(25) Wu, L.; Hu, H.; Xu, Y.; Jiang, S.; Chen, M.; Zhong, Q.; Yang, D.; Liu, Q.; Zhao, Y.; Sun, B.; Zhang, Q.; Yin, Y. From Nonluminescent Cs_4PbX_6 (X = Cl, Br, I) Nanocrystals to Highly Luminescent CsPbX3 Nanocrystals: Water-Triggered Transformation

through a CsX-Stripping Mechanism. *Nano Lett.* **2017**, *17*, 5799−5804.
(26) Zhang, X.; Bai, X.; Wu, H.; Zhang, X.; Sun, C.; Zhang, Y.; Zhang, W.; Zheng, W.; Yu, W. W.; Rogach, A. L. Water-Assisted Size and Shape Control of $CsPbBr_3$ Perovskite Nanocrystals. *Angew. Chem., Int. Ed.* **2018**, *57*, 3337−3342.
(27) Wang, C.; Huang, H.; Weng, B.; Verhaeghe, D.; Keshavarz, M.; Jin, H.; Liu, B.; Xie, H.; Ding, Y.; Gao, Y.; Yuan, H.; Steele, J. A.; Hofkens, J.; Roeffaers, M. B. J. Planar Heterojunction Boosts Solar-Driven Photocatalytic Performance and Stability of Halide Perovskite Solar Photocatalyst Cell. *Appl. Catal., B* **2022**, *301*, 120760.
(28) Wang, Y.; Zhang, R.; Yue, Y.; Yan, S.; Zhang, L.; Chen, D. Room Temperature Synthesis of $CsPbX_3$ (X = Cl, Br, I) Perovskite Quantum Dots by Water-Induced Surface Crystallization of Glass. *J. Alloys Compd.* **2020**, *818*, 152872.
(29) Govinda, S.; Kore, B. P.; Swain, D.; Hossain, A.; De, C.; Guru Row, T. N.; Sarma, D. D. Critical Comparison of $FAPbX_3$ and $MAPbX_3$ (X = Br and Cl): How Do They Differ? *J. Phys. Chem. C* **2018**, *122*, 13758−13766.
(30) Li, G.; Zhang, Y.; Zhao, X.; Lin, J.; She, C.; Liu, S.; Jing, C.; Cheng, Y.; Chu, J. Bismuth-Based Lead-Free Perovskite Film for Highly Sensitive Detection of Ammonia Gas. *Sens. Actuators, B* **2021**, *345*, 130298.
(31) Yang, X.; Zhang, X.; Deng, J.; Chu, Z.; Jiang, Q.; Meng, J.; Wang, P.; Zhang, L.; Yin, Z.; You, J. Efficient Green Light-Emitting Diodes Based on Quasi-Two-Dimensional Composition and Phase Engineered Perovskite with Surface Passivation. *Nat. Commun.* **2018**, *9*, 570.
(32) Qu, R.; Zou, L.; Qi, X.; Liu, C.; Zhao, W.; Yan, J.; Zhang, Z.; Wu, Y. Changing the Shape and Optical Properties of $CsPbBr_3$ Perovskite Nanocrystals with Hydrohalic Acids Using a Room-Temperature Synthesis Process. *CrystEngComm* **2020**, *22*, 1853−1857.
(33) Grechko, M.; Bretschneider, S. A.; Vietze, L.; Kim, H.; Bonn, M. Vibrational Coupling between Organic and Inorganic Sublattices of Hybrid Perovskites. *Angew. Chem., Int. Ed.* **2018**, *57*, 13657−13661.
(34) Pan, J.; Quan, L. N.; Zhao, Y.; Peng, W.; Murali, B.; Sarmah, S. P.; Yuan, M.; Sinatra, L.; Alyami, N. M.; Liu, J.; Yassitepe, E.; Yang, Z.; Voznyy, O.; Comin, R.; Hedhili, M. N.; Mohammed, O. F.; Lu, Z. H.; Kim, D. H.; Sargent, E. H.; Bakr, O. M. Highly Efficient Perovskite-Quantum-Dot Light-Emitting Diodes by Surface Engineering. *Adv. Mater.* **2016**, *28*, 8718−8725.
(35) Sun, C.; Jiang, Y.; Cui, M.; Qiao, L.; Wei, J.; Huang, Y.; Zhang, L.; He, T.; Li, S.; Hsu, H.-Y.; Qin, C.; Long, R.; Yuan, M. High-Performance Large-Area Quasi-2D Perovskite Light-Emitting Diodes. *Nat. Commun.* **2021**, *12*, 2207.
(36) Li, N.; Lei, F.; Ji, X.; Yin, L.; Shi, Y. Synthesis of Self-Assembled One-Dimensional Perovskite Nanobelt Passivated by Homophthalic Acid and Application in WLED. *J. Lumin.* **2022**, *241*, 118531.
(37) Gonzalez-Carrero, S.; Espallargas, G. M.; Galian, R. E.; Pérez-Prieto, J. Blue-Luminescent Organic Lead Bromide Perovskites: Highly Dispersible and Photostable Materials. *J. Mater. Chem. A* **2015**, *3*, 14039−14045.
(38) Clinckemalie, L.; Valli, D.; Roeffaers, M. B. J.; Hofkens, J.; Pradhan, B.; Debroye, E. Challenges and Opportunities for $CsPbBr_3$ Perovskites in Low- and High-Energy Radiation Detection. *ACS Energy Lett.* **2021**, *6*, 1290−1314.
(39) Reus, M. A.; Reb, L. K.; Weinzierl, A. F.; Weindl, C. L.; Guo, R.; Xiao, T.; Schwartzkopf, M.; Chumakov, A.; Roth, S. V.; Müller-Buschbaum, P. Time-Resolved Orientation and Phase Analysis of Lead Halide Perovskite Film Annealing Probed by In Situ GIWAXS. *Adv. Opt. Mater.* **2022**, *10*, 2102722.
(40) Levchuk, I.; Osvet, A.; Tang, X.; Brandl, M.; Perea, J. D.; Hoegl, F.; Matt, G. J.; Hock, R.; Batentschuk, M.; Brabec, C. J. Brightly Luminescent and Color-Tunable Formamidinium Lead Halide Perovskite $FAPbX_3$ (X = Cl, Br, I) Colloidal Nanocrystals. *Nano Lett.* **2017**, *17*, 2765−2770.
(41) Na Quan, L.; Ma, D.; Zhao, Y.; Voznyy, O.; Yuan, H.; Bladt, E.; Pan, J.; García de Arquer, F. P.; Sabatini, R.; Piontkowski, Z.; Emwas, A.-H.; Todorović, P.; Quintero-Bermudez, R.; Walters, G.; Fan, J. Z.; Liu, M.; Tan, H.; Saidaminov, M. I.; Gao, L.; Li, Y.; Anjum, D. H.; Wei, N.; Tang, J.; McCamant, D. W.; Roeffaers, M. B. J.; Bals, S.; Hofkens, J.; Bakr, O. M.; Lu, Z.-H.; Sargent, E. H. Edge Stabilization in Reduced-Dimensional Perovskites. *Nat. Commun.* **2020**, *11*, 170.
(42) Liu, E.; Lei, L.; Xie, B.; Xu, S. Engineering $CsPbBr_3$ Perovskite from 2D Nanoplatelets to 0D Quantum Dots via Polar Solvent Post-Treatment. *Opt. Mater.* **2022**, *125*, 112120.
(43) Zhu, W.; Shen, J.; Li, M.; Yang, K.; Bu, W.; Sun, Y.-Y.; Shi, J.; Lian, J. Kinetically Controlled Growth of Sub-Millimeter 2D Cs_2SnI_6 Nanosheets at the Liquid−Liquid Interface. *Small* **2021**, *17*, 2006279.
(44) Feng, A.; Jiang, X.; Zhang, X.; Zheng, X.; Zheng, W.; Mohammed, O. F.; Chen, Z.; Bakr, O. M. Shape Control of Metal Halide Perovskite Single Crystals: From Bulk to Nanoscale. *Chem. Mater.* **2020**, *32*, 7602−7617.
(45) Duim, H.; Fang, H.-H.; Adjokatse, S.; ten Brink, G. H.; Marques, M. A. L.; Kooi, B. J.; Blake, G. R.; Botti, S.; Loi, M. A. Mechanism of Surface Passivation of Methylammonium Lead Tribromide Single Crystals by Benzylamine. *Appl. Phys. Rev.* **2019**, *6*, 031401.
(46) Looby, D.; Griffiths, J. B. Fixed Bed Porous Glass Sphere (Porosphere) Bioreactors for Animal Cells. *Cytotechnology* **1988**, *1*, 339−346.
(47) Li, M.; Gao, Q.; Liu, P.; Liao, Q.; Zhang, H.; Yao, J.; Hu, W.; Wu, Y.; Fu, H. Amplified Spontaneous Emission Based on 2D Ruddlesden−Popper Perovskites. *Adv. Funct. Mater.* **2018**, *28*, 1707006.
(48) Wang, H.; Ye, F.; Sun, J.; Wang, Z.; Zhang, C.; Qian, J.; Zhang, X.; Choy, W. C. H.; Sun, X. W.; Wang, K.; Zhao, W. Efficient $CsPbBr_3$ Nanoplatelet-Based Blue Light-Emitting Diodes Enabled by Engineered Surface Ligands. *ACS Energy Lett.* **2022**, *7*, 1137−1145.
(49) Jin, Y.; Wang, Z.-K.; Yuan, S.; Wang, Q.; Qin, C.; Wang, K.-L.; Dong, C.; Li, M.; Liu, Y.; Liao, L.-S. Synergistic Effect of Dual Ligands on Stable Blue Quasi-2D Perovskite Light-Emitting Diodes. *Adv. Funct. Mater.* **2020**, *30*, 1908339.
(50) Wang, F.; Wang, Z.; Sun, W.; Wang, Z.; Bai, Y.; Hayat, T.; Alsaedi, A.; Tan, Z. High Performance Quasi-2D Perovskite Sky-Blue Light-Emitting Diodes Using a Dual-Ligand Strategy. *Small* **2020**, *16*, 2002940.
(51) Zhu, W.; Xin, G.; Scott, S. M.; Xu, W.; Yao, T.; Gong, B.; Wang, Y.; Li, M.; Lian, J. Deciphering the Degradation Mechanism of the Lead-Free All Inorganic Perovskite Cs_2SnI_6. *npj Mater. Degrad.* **2019**, *3*, 7.
(52) Lyu, B.; Guo, X.; Gao, D.; Kou, M.; Yu, Y.; Ma, J.; Chen, S.; Wang, H.; Zhang, Y.; Bao, X. Highly-Stable Tin-Based Perovskite Nanocrystals Produced by Passivation and Coating of Gelatin. *J. Hazard. Mater.* **2021**, *403*, 123967.
(53) Cao, J.; Tao, S. X.; Bobbert, P. A.; Wong, C.-P.; Zhao, N. Interstitial Occupancy by Extrinsic Alkali Cations in Perovskites and Its Impact on Ion Migration. *Adv. Mater.* **2018**, *30*, 1707350.
(54) Prasanna, R.; Gold-Parker, A.; Leijtens, T.; Conings, B.; Babayigit, A.; Boyen, H.-G.; Toney, M. F.; McGehee, M. D. Band Gap Tuning via Lattice Contraction and Octahedral Tilting in Perovskite Materials for Photovoltaics. *J. Am. Chem. Soc.* **2017**, *139*, 11117−11124.
(55) Dang, Z.; Dhanabalan, B.; Castelli, A.; Dhall, R.; Bustillo, K. C.; Marchelli, D.; Spirito, D.; Petralanda, U.; Shamsi, J.; Manna, L.; Krahne, R.; Arciniegas, M. P. Temperature-Driven Transformation of $CsPbBr_3$ Nanoplatelets into Mosaic Nanotiles in Solution through Self-Assembly. *Nano Lett.* **2020**, *20*, 1808−1818.
(56) Li, L.; Pandey, A.; Werder, D. J.; Khanal, B. P.; Pietryga, J. M.; Klimov, V. I. Efficient Synthesis of Highly Luminescent Copper Indium Sulfide-Based Core/Shell Nanocrystals with Surprisingly Long-Lived Emission. *J. Am. Chem. Soc.* **2011**, *133*, 1176−1179.
(57) Li, S.; Zhang, Y.; Yang, W.; Liu, H.; Fang, X. 2D Perovskite $Sr_2Nb_3O_{10}$ for High-Performance UV Photodetectors. *Adv. Mater.* **2020**, *32*, 1905443.

(58) Peng, X.; Yan, C.; Chun, F.; Li, W.; Fu, X.; Yang, W. A Review of Low-Dimensional Metal Halide Perovskites for Blue Light Emitting Diodes. *J. Alloys Compd.* **2021**, *883*, 160727.
(59) Yan, D.; Shi, T.; Zang, Z.; Zhou, T.; Liu, Z.; Zhang, Z.; Du, J.; Leng, Y.; Tang, X. Ultrastable $CsPbBr_3$ Perovskite Quantum Dot and Their Enhanced Amplified Spontaneous Emission by Surface Ligand Modification. *Small* **2019**, *15*, 1901173.
(60) Chen, P.; Bai, Y.; Wang, S.; Lyu, M.; Yun, J.-H.; Wang, L. In Situ Growth of 2D Perovskite Capping Layer for Stable and Efficient Perovskite Solar Cells. *Adv. Funct. Mater.* **2018**, *28*, 1706923.
(61) Fassl, P.; Zakharko, Y.; Falk, L. M.; Goetz, K. P.; Paulus, F.; Taylor, A. D.; Zaumseil, J.; Vaynzof, Y. Effect of Density of Surface Defects on Photoluminescence Properties in $MAPbI_3$ Perovskite Films. *J. Mater. Chem. C* **2019**, *7*, 5285−5292.
(62) Wright, A. D.; Verdi, C.; Milot, R. L.; Eperon, G. E.; Pérez-Osorio, M. A.; Snaith, H. J.; Giustino, F.; Johnston, M. B.; Herz, L. M. Electron−Phonon Coupling in Hybrid Lead Halide Perovskites. *Nat. Commun.* **2016**, *7*, 11755.
(63) Keshavarz, M.; Ottesen, M.; Wiedmann, S.; Wharmby, M.; Küchler, R.; Yuan, H.; Debroye, E.; Steele, J. A.; Martens, J.; Hussey, N. E.; Bremholm, M.; Roeffaers, M. B. J.; Hofkens, J. Tracking Structural Phase Transitions in Lead-Halide Perovskites by Means of Thermal Expansion. *Adv. Mater.* **2019**, *31*, 1900521.
(64) Kim, H.; Ra, H. N.; Kim, J. S.; Paek, S.-H.; Park, J.; Kim, Y. C. Improved Performance of Flexible Perovskite Light-Emitting Diodes with Modified PEDOT:PSS Hole Transport Layer. *J. Ind. Eng. Chem.* **2020**, *90*, 117−121.
(65) Li, J.; Wang, X.; Tan, Y.; Liang, D.; Zou, Y.; Cai, L.; Wu, T.; Wen, K.; Wang, Y.; Li, Y.; Song, T.; Wang, L.; Sun, B. Strontium Ion B-Site Substitution for Spectral-Stable Blue Emitting Perovskite Light-Emitting Diodes. *Adv. Opt. Mater.* **2020**, *8*, 2001073.
(66) Sanchez, R. S.; de la Fuente, M. S.; Suarez, I.; Muñoz-Matutano, G.; Martinez-Pastor, J. P.; Mora-Sero, I. Tunable Light Emission by Exciplex State Formation between Hybrid Halide Perovskite and Core/Shell Quantum Dots: Implications in Advanced LEDs and Photovoltaics. *Sci. Adv.* **2016**, *2*, No. e1501104.
(67) Favre-Nicolin, V.; Černý, R. FOX, 'free Objects for Crystallography': A Modular Approach to Ab Initio Structure Determination from Powder Diffraction. *J. Appl. Crystallogr.* **2002**, *35*, 734−743.
(68) Rodríguez-Carvajal, J. Recent Advances in Magnetic Structure Determination by Neutron Powder Diffraction. *Physica B: Condensed Matter* **1993**, *192*, 55−69.
(69) Levy, H. A.; Peterson, S. W. Neutron Diffraction Determination of the Crystal Structure of Ammonium Bromide in Four Phases1. *J. Am. Chem. Soc.* **1953**, *75*, 1536−1542.
(70) Gražulis, S.; Chateigner, D.; Downs, R. T.; Yokochi, A. F. T.; Quirós, M.; Lutterotti, L.; Manakova, E.; Butkus, J.; Moeck, P.; Le Bail, A. Crystallography Open Database − an Open-Access Collection of Crystal Structures. *J. Appl. Crystallogr.* **2009**, *42*, 726−729.